Dust Production and Depletion in Evolved Planetary Systems

J. Farihi¹*, R. van Lieshout², P. W. Cauley^{3,11}, E. Dennihy⁴, K. Y. L. Su⁵, S. J. Kenyon⁶, T. G. Wilson^{1,7}, O. Toloza⁸, B. T. Gänsicke^{8,9}, T. von Hippel¹⁰, S. Redfield¹¹, J. H. Debes¹², S. Xu¹³, L. Rogers², A. Bonsor², A. Swan¹, A. F. Pala⁸, W. T. Reach¹³

31 August 2018

ABSTRACT

The infrared dust emission from the white dwarf GD 56 is found to rise and fall by 20% peak-to-peak over $11.2\,\mathrm{yr}$, and is consistent with ongoing dust production and depletion. It is hypothesized that the dust is produced via collisions associated with an evolving dust disk, temporarily increasing the emitting surface of warm debris, and is subsequently destroyed or assimilated within a few years. The variations are consistent with debris that does not change temperature, indicating that dust is produced and depleted within a fixed range of orbital radii. Gas produced in collisions may rapidly re-condense onto grains, or may accrete onto the white dwarf surface on viscous timescales that are considerably longer than Poynting-Robertson drag for micron-sized dust. This potential delay in mass accretion rate change is consistent with multi-epoch spectra of the unchanging Ca II and Mg II absorption features in GD 56 over 15 yr, although the sampling is sparse. Overall these results indicate that collisions are likely to be the source of dust and gas, either inferred or observed, orbiting most or all polluted white dwarfs.

Key words: circumstellar matter— planetary systems— stars: individual (GD 56)— white dwarfs

1 INTRODUCTION

Observable and real-time changes in exoplanetary systems hold important clues for dynamical processes during their birth and long-term evolution, where the number of variable systems is likely to increase owing to large ground- and space-based surveys. Sensitive monitoring of giant planetary and substellar atmospheres can reveal periodic features such as rotation, atmospheric wind speeds, and global weather patterns (Snellen et al. 2014; Louden & Wheatley 2015; Apai et al. 2017). Smaller major and minor exoplanetary bodies are typically out of reach for real-time monitoring, but those that

* E-mail: j.farihi@ucl.ac.uk

actively produce debris can generate sufficient area to be detected via absorption or emission and studied over time. Such systems have the potential to constrain the bigger picture of planet formation and evolution, especially if they exhibit secular changes, non-periodic events, or signposts of important evolutionary phases such as the Late Heavy Bombardment.

Active exo-cometary populations are known in a handful of systems via transient absorption in optical and ultraviolet spectra (Kiefer et al. 2014a,b; Welsh & Montgomery 2018), while *Kepler* data now includes convincing transits of individual exo-comets in at least one system (Rappaport et al. 2018). The dramatic and irregular flux changes measured towards KIC 8462852 are also broadly consistent with an exo-cometary origin (Boyajian et al.

¹Department of Physics and Astronomy, University College London, London WC1E 6BT, UK

²Institute of Astronomy, University of Cambridge, Cambridge CB3 0HA, UK

³School of Earth and Space Exploration, Arizona State University, Tempe, AZ 85287, USA

⁴Physics and Astronomy Department, University of North Carolina at Chapel Hill, Chapel Hill, NC 27599, USA

⁵Steward Observatory, University of Arizona, Tucson AZ 85721, USA

⁶Smithsonian Astrophysical Observatory, Cambridge, MA 02138, USA

⁷Isaac Newton Group of Telescopes, E-38700 Santa Cruz de La Palma, Spain

⁸Department of Physics, University of Warwick, Coventry CV4 7AL, UK

⁹Centre for Exoplanets and Habitability, University of Warwick, Coventry CV4 7AL, UK

¹⁰Physical Sciences Department, Embry-Riddle Aeronautical University, Daytona Beach FL 32114, USA

¹¹Astronomy Department and Van Vleck Observatory, Wesleyan University, Middletown 06459, USA

¹²Space Telescope Science Institute, Baltimore, MD 21218, USA

¹³Gemini Observatory, Northern Operations, Hilo, HI 96720, USA

¹⁴SOFIA-USRA, NASA Ames Research Center, Moffett Field, CA 94035, USA

2 J. Farihi et al.

2018; Wyatt et al. 2018). The inner and terrestrial planet-analog regions are more challenging to detect in general due to their host star proximity, but sensitivity to compact orbits has enabled *Kepler* to detect transits from a trio of rocky planets via tailing debris clouds associated with their short periods and thus irradiation-driven mass loss (van Lieshout & Rappaport 2017). Analogous processes may contribute to the transit light curves of the polluted white dwarf WD 1145+017 (hereafter WD 1145; Vanderburg et al. 2015; Gänsicke et al. 2016; Rappaport et al. 2016).

Exoplanetary system variability has also been observed in light curves via emission, including a few spectacular examples of infrared flux changes associated with the terrestrial-planet forming regions (Melis et al. 2012; Meng et al. 2014). And within the former terrestrial zones of A-type and similar stars, there is myriad evidence for rocky planetesimal activity via the evolved planetary systems orbiting and polluting white dwarf stars (see Farihi 2016 and references therein). The first clear evidence of any variability in these systems emerged via changes in disk line emission (Gänsicke et al. 2008), and preceded transit detections by several years. Similar changes have now been documented for five disks via gas emission or absorption (Wilson et al. 2014; Manser et al. 2016a,b; Dennihy et al. 2018), including WD 1145 (Redfield et al. 2017; Cauley et al. 2018), but to date only a single white dwarf system has been shown to vary in the infrared.

SDSS J095904.69-020047.6 (hereafter SDSS 0959) was reported to show a drop in $3-5\,\mu m$ infrared flux by around 35% in less than 300 d (Xu & Jura 2014) based on the comparison of its warm Spitzer IRAC discovery fluxes (Farihi et al. 2012a) to measurements made with WISE. Xu & Jura (2014) surmised the drop in flux was likely due to a change in the inner disk radius from an impact or instability, causing a few percent of the entire disk mass to be accreted within the duration of the observed change, and suggest that the resulting accretion rate increase could lead to an observable difference in the photospheric metal abundance on similarly-short timescales.

This paper reports long-term, $3-5\,\mu m$ infrared flux variations in the polluted white dwarf GD 56 (= WD 0408–041), a hydrogen atmosphere (DA-type) star with $T_{\rm eff}\approx 15\,000\,{\rm K}$ and a cooling age around 200 Myr (Gianninas et al. 2011). The variability in the infrared is presented together with optical spectroscopy that reveals constant, photospheric metal absorption over a similar timescale. Infrared data are comprised of nine *Spitzer* observational epochs spanning 11.2 yr from 2006 to 2017, and are supplemented by multiepoch *WISE* data from 2010 and 2014–2017. There has been one substantial increase of at least 20%, and what appear to be two decaying trends of similar magnitude, all taking place over several years each. These changes are interpreted as the production (increase) of dust clouds, and their subsequent depletion (decrease), where possible scenarios may also account for the flux decrease at SDSS 0959.

The rest of the paper is organized as follows. Section two describes the infrared data, where the analysis includes both absolute flux measurements and differential photometry using field stars, and the spectroscopic data that indicate no appreciable changes to the inferred metal accretion rate. Section three describes the (weak) constraints on disk models based on the data, as well as theoretical considerations, and discusses possible model families for GD 56 and dusty white dwarfs in general. Section four gives the summary and outlook.

2 OBSERVATIONS AND ANALYSIS

The following section describes the two types of observational data for GD 56 used in this study. The first are infrared photometric observations of excess emission that track the properties of warm circumstellar dust, and include data taken with the *Spitzer Space Telescope* (Werner et al. 2004), the *Wide-field Infrared Survey Explorer* (WISE; Wright et al. 2010), and ground-based *JHK* photometry. The second are medium- to high-resolution optical spectra that trace the abundance of atmospheric metals that result from disk accretion. The infrared and optical data sets were independently obtained by several teams for various purposes; there is no correlated timing between any. In particular, the *Spitzer* and optical data are both irregularly distributed in time, but the NEOWISE data have semi-regular cadence.

2.1 Infrared Photometry

Multi-epoch *Spitzer* IRAC (Fazio et al. 2004) data were retrieved from the archive, where they were first processed by the *Spitzer* Science Center via pipeline S18.18.0 for cryogenic data, or S19.2.0 for warm mission data. There are six programs 1 that targeted GD 56 between 2006 Sep and 2017 Dec, and that yield nine total epochs of data in either channel 1 at 3.6 μ m or channel 2 at 4.5 μ m. This study focuses on the two shortest wavelength bandpass data, as the four most recent epochs were taken post-cryogen, and moreover they are directly comparable to channels 1 and 2 of *WISE*. Together these collective data yield a compelling data set.

Fluxes at 3.6 and 4.5 µm were each measured in two ways; first on single exposure, basic calibrated data (BCD) frames, and second on mosaics created using MOPEX following the best practices as detailed in the IRAC Instrument Handbook v2.1. Both IRAF and APEX were used to perform aperture photometry on GD 56, where photometry was executed using aperture radii of 2-3 native pixels and sky annuli of 12-20 native pixels with appropriate aperture corrections. The signal-to-noise ratios (S/N) of these data are on the order of several hundred or greater and thus contribute negligible measurement error to the flux uncertainties, and thus the total errors are limited by the calibration uncertainty of the instrument ($\approx 2\%$; Reach et al. 2005). As these results only depend on the changing flux for a source within a given passband, the calibration uncertainty is irrelevant. The different methods of measuring flux via aperture photometry were all found to agree to $\ll 1\%$, and the adopted values are plotted in Figure 1 and listed in Table 1.

To better constrain the significance of the actual changes, the IRAC image mosaics were used to perform differential photometry on GD 56. The brightest five, isolated field stars with good overlap (mosaic) coverage were chosen for relative flux measurements, and are all around 2–5 times fainter than the science target in both channels. Flux ratios between each field star and the science target were determined using APEX aperture photometry as above with r=2 native pixels. The uncertainties of individual relative fluxes were calculated using the quadrature sum of the measurement errors for each pair. For each IRAC epoch the weighted mean and error of these five ratios are plotted in Figure 2, after normalization across all epochs. While these relative fluxes appear to strongly confirm the real nature of the flux changes in GD 56, the measurement errors alone may underestimate the true uncertainty as these do not account for potential bona fide variations in the comparison field stars.

¹ ID# 275, 40369, 90095, 10032, 10175, 13216

Table 1. Infrared Observations of GD 56

Date	Ch 1: 3.55 μm (mJy)	Spitzer IRAC Ch 2: 4.49 μm (mJy)	Ch 2 / Ch 1					
2006.09.20	1.074 ± 0.019	1.214 ± 0.023	1.130 ± 0.030					
2007.10.17	1.037 ± 0.019	1.177 ± 0.022	1.134 ± 0.030					
2007.10.18	1.025 ± 0.018	1.187 ± 0.023	1.158 ± 0.031					
2007.10.23	1.029 ± 0.019	1.172 ± 0.022	1.139 ± 0.031					
2008.03.10	1.058 ± 0.019	1.174 ± 0.022	1.110 ± 0.030					
2013.10.30		1.322 ± 0.025						
2014.05.15	1.138 ± 0.020	1.269 ± 0.024	1.115 ± 0.030					
2014.12.19	1.106 ± 0.020	1.233 ± 0.023	1.115 ± 0.030					
2017.12.06	0.983 ± 0.018	1.068 ± 0.020	1.087 ± 0.029					
	WISE + NEOWISE							
	Ch 1: 3.35 μm	Ch 2: 4.60 μm	Ch 2 / Ch 1					
	(mJy)	(mJy)						
2010.02.13	0.869 ± 0.013	1.090 ± 0.017	1.254 ± 0.027					
2010.08.22	0.835 ± 0.015	1.065 ± 0.018	1.275 ± 0.031					
2014.02.16	1.048 ± 0.012	1.278 ± 0.022	1.219 ± 0.025					
2014.08.26	1.001 ± 0.013	1.223 ± 0.022	1.222 ± 0.027					
2015.02.11	0.993 ± 0.012	1.233 ± 0.023	1.242 ± 0.028					
2015.08.23	0.959 ± 0.012	1.138 ± 0.023	1.187 ± 0.028					
2016.02.05	0.952 ± 0.011	1.162 ± 0.018	1.220 ± 0.024					
2016.08.21	0.920 ± 0.012	1.130 ± 0.022	1.228 ± 0.029					
2017.02.03	0.888 ± 0.012	1.111 ± 0.021	1.251 ± 0.029					
2017.02.06	0.881 ± 0.012	1.099 ± 0.033	1.247 ± 0.041					
2017.08.23	0.845 ± 0.012	0.987 ± 0.021	1.168 ± 0.030					
	Ground-Based Photometry							
	J	H	K					
	(mag)	(mag)	(mag)					
1998.10.12 ^a	15.87 ± 0.06	15.99 ± 0.13	15.44 ± 0.18					
2006.10.09 ^b	15.85 ± 0.05	15.75 ± 0.05	15.13 ± 0.05					
2014.10.03 ^c	15.96 ± 0.03	15.76 ± 0.04	15.10 ± 0.04					
2016.10.10 ^c	15.95 ± 0.03	15.77 ± 0.03	15.12 ± 0.03					
2017.01.31 ^c	15.92 ± 0.03	15.80 ± 0.04	15.16 ± 0.03					

^a 2MASS (Skrutskie et al. 2006).

Additional multi-epoch infrared photometry was taken by WISE and retrieved from the AllWISE and NEOWISE source catalogs. During the cryogenic mission there were two sets of observations for GD 56 (2010 Feb and Aug), and during NEOWISE (Mainzer et al. 2011) there have been an additional nine, regularly-spaced epochs (2014 Feb to 2017 Aug). Each epoch of data consists of approximately one dozen individual measurements and errors, and for each, both the fluxes and their corresponding errors were determined by weighted average. Typical uncertainties in mean WISE flux are comparable to the IRAC data at $\approx 2\%$, and combined data points for each epoch are shown in Figure 1. The NEOWISE data are essentially contiguous with a cadence near either 165 or 195 d, and the individual measurements and errors are shown in Figure 3.

All absolute flux measurements are plotted in Figure 1 as a function of date, as well as the flux ratios between the longer and shorter wavelength channels. Because the two spacecraft have similar but still distinct filter sets, the channel 2:1 flux ratios of IRAC and WISE cannot be directly compared. Furthermore, while Spitzer and WISE share a network of infrared calibration standards, the absolute scales differ by up to a few per cent (Jarrett et al. 2011). The

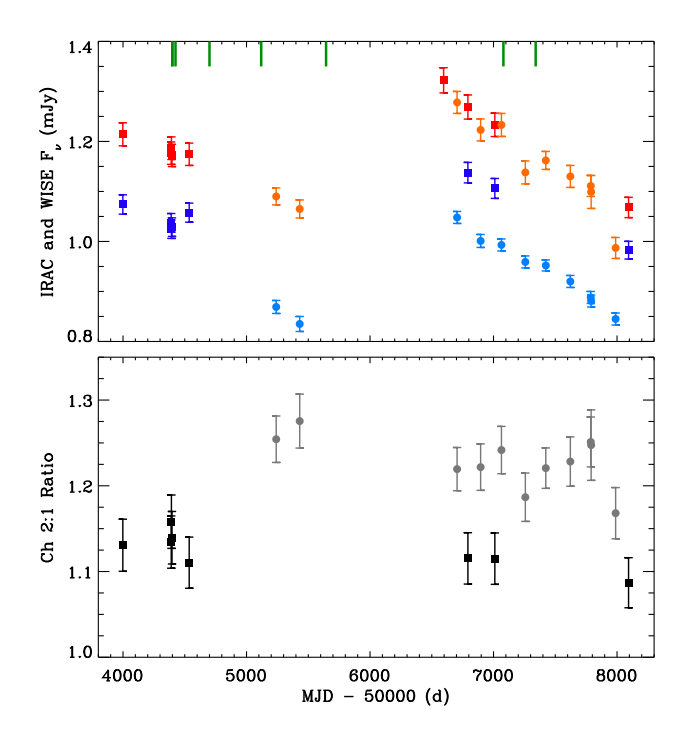


Figure 1. Flux-calibrated infrared data for GD 56 over 11.2 yr as measured by Spitzer and WISE in their two shortest wavelength channels. In the upper panel, the IRAC and WISE fluxes with errors are given as squares and circles, respectively, with blue hues indicating channel 1 centered near 3.5 µm, and red hues for channel 2 centered near $4.5\,\mu m$. The corresponding pairs of bandpass filters on each spacecraft are similar, but vary by a few percent in isophotal wavelength and by several percent in bandwidth (Jarrett et al. 2011). All IRAC photometry has S/N \gg 100 so that the measurements are limited by the $\approx 2\%$ calibration uncertainty of the instrument. Each WISE flux is the weighted mean and error of multi-epoch photometry in AllWISE and NEOWISE, where each epoch typically consists of 12 individual measurements. The green vertical bars at the top of the panel indicate eight dates where spectroscopic observations of GD 56 were taken. The lower panel plots the channel 2:1 flux ratios, with IRAC data in black and the WISE ratios in grey. These ratios indicate that the temperature of the emitting dust - and hence its location - does not appear to be changing significantly.

 $2-20\,\mu m$ continuum emission from GD 56 has previously been shown to be consistent with a $T=1000\,K$ blackbody (Jura et al. 2007), and this model flux can be convolved with the filter bandpasses of both spacecraft, providing an estimated transformation between *WISE* and IRAC fluxes and flux ratios. Such a transformation can roughly reproduce both the fluxes and flux ratios where observations occurred most closely together in time. The best such mapping is achieved near a blackbody temperature of 900 K, where all fluxes and flux ratios between spacecraft are then within 1σ .

Lastly, GD 56 was observed in the $1-2.5\,\mu m$ region between 2014 Oct and 2017 Jan using the Wide Field Camera (WFCAM) on the United Kingdom Infrared Telescope (UKIRT) on Mauna Kea (Rogers et al. 2018, in prep.). For each of the *JHK* bands, three epochs of imaging were obtained using a five-point dither pattern and a total exposure time of 75 s. The infrared images were pipeline processed by the Cambridge Astronomical Survey Unit to produce photometrically and astrometrically calibrated images and source catalogs (Hodgkin et al. 2009). For each observing epoch, the weighted mean *JHK* magnitudes for GD 56 were taken from

^b IRTF; SpeX (Farihi 2009).

^c UKIRT; WFCAM (this work).

4 J. Farihi et al.

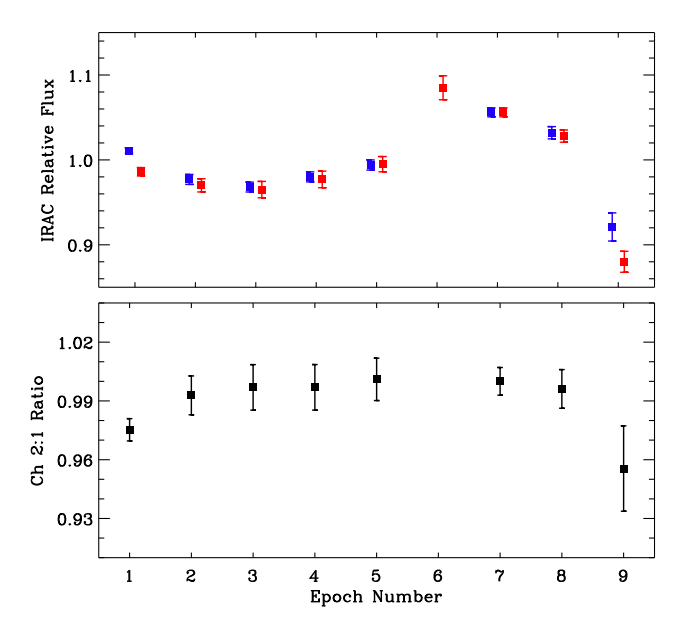


Figure 2. Relative IRAC fluxes obtained via differential photometry for GD 56 in both channels using five comparison stars in common for all nine Spitzer epochs. Symbols and colors are the same as in Figure 1, and there are no data available in IRAC channel 1 for the sixth epoch (program ID 90095). The upper panel plots the weighted mean and error of five differential photometric measurements per epoch, where the values are normalized so that the average of all epochs is 1.0 in each channel, and with small horizontal offsets between the 3.6 and 4.5 µm data points for clarity. These relative fluxes were measured for all sources identically as described in Section 2.1, and include only errors propagated based on measurement uncertainties (i.e. S/N). Any intrinsic variation among the comparison stars is not accounted for here, but ignoring this possibility yields a difference of 23% between the minimum and maximum differential measurements, at over 10 o. The lower panel plots the ratios of the channel 2:1 differential photometry from the upper panel, and again suggests the temperature of the dust is not changing over the long timescale probed by these widely-spaced observations.

the output catalogs, and to the photometric measurement errors was added a systematic uncertainty typical of infrared arrays (e.g. Leggett et al. 2006). The resulting WFCAM photometry is reported in Table 1, together with previously published $1-2.5\,\mu m$ data. All the measured $\it JHK$ photometry are consistent within $2\sigma-3\sigma$ in each of the bandpasses, and the values themselves generally vary by less than around 6%.

2.2 Optical Spectroscopy

Echelle spectroscopy of GD 56 with sufficient resolution to detect atmospheric metals was executed using five separate instruments over ten epochs between the photospheric metal discovery spectrum in 2000 Sep (Koester et al. 2005) and 2015 Nov. The relevant observational details are summarized in Table 2. Individual exposures were extracted, combined as appropriate, and calibrated according to the facility-recommended methods and software (e.g. Kelson et al. 2000; Kelson 2003; Freudling et al. 2013). Spectra were all continuum normalized and portions of each are shown in Figure 4. The Keck HIRES spectrum taken on 2011 Mar 23 is a single exposure that was completed prior to the end of twilight and suffers from high sky counts – including emission lines – in all

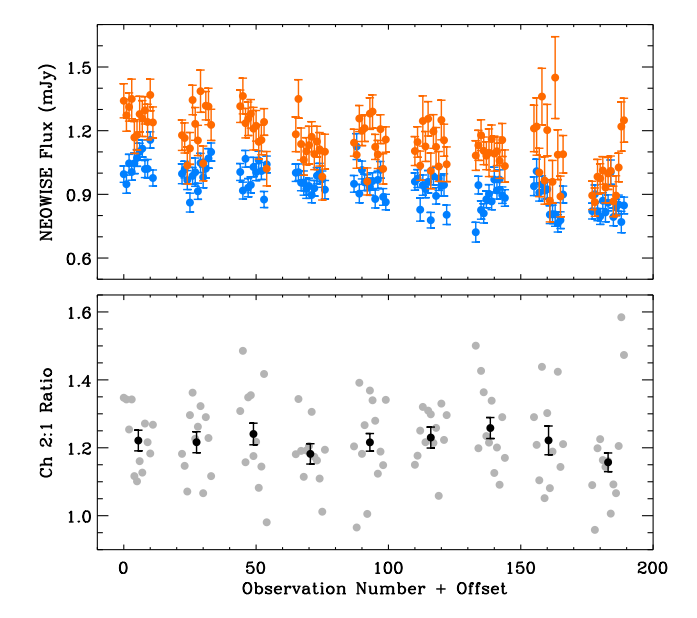


Figure 3. All NEOWISE measurements for GD 56 in channels 1 and 2, where the colors are the same as in Figure 1. These are 110 individual fluxes and errors, where typically one dozen are obtained during a single epoch spanning many hours, and epochs are separated by around 180 d on average. The data are displayed in chronological order by number, with distinct epochs offset along the x-axis. The dimming trend is clear in the raw data of both the 3.4 and 4.6 μ m channels, but the flux ratio in the bottom panel does not show any significant change or trend, despite the regular and roughly semi-annual sampling of this observational subset. The black data points with error bars are the weighted mean and weighted error of the individual flux ratios (and their errors, not shown) plotted in in grey.

relevant orders. For the remaining spectra there were no significant observing or instrument conditions that may have affected the data.

Equivalent widths (W_{λ}) for Ca II K 3934 Å and Mg II 4481 Å are calculated for each epoch of spectroscopy and given in Table 2 and plotted in Figure 5. It is noteworthy that the Ca II H 3968 Å line is not detected at a significant level in any of the spectra, however, this transition is contained within the strong and broad H ϵ absorption feature. The spectral regions surrounding the lines are first normalized using a low-order polynomial, and the wavelength range used for the W_{λ} integration is shown in grey in Figure 4. Uncertainties for the W_{λ} measurements are a combination of normalized flux errors and an estimate of the systematic uncertainty due to extraction and normalization of the spectra. Normalized flux uncertainties are calculated by taking the standard deviation of 2 Å segments on either side of the line of interest. The systematic uncertainty is set equal to the normalized flux uncertainty, and is summed in quadrature with the normalized flux errors to produce the total W_{λ} error (effectively increasing the total uncertainty by $\sqrt{2}$).

All spectra were fitted using white dwarf atmospheric models (Koester 2010) to determine abundances for calcium and magnesium. The stellar parameters of GD 56 were fixed at $T_{\rm eff}=15\,000\,{\rm K}$ and log g=8.0; this temperature is within 1% of the average literature value (Koester et al. 2005; Koester 2009; Gianninas et al. 2011), and the surface gravity agrees well with the *Gaia* DR2 parallax ($\varpi=14.07\pm0.05$ mas; Gaia Collaboration et al. 2018) distance of 71.07 ± 0.25 pc. The fitting process worked well for all spectra with the exception of the 2011 HIRES data set, where both the Mg II partially-resolved triplet and Ca II K line features are too nar-

Table 2. Summary of Blue Optical Spectroscopic Observations and Analyses for GD 56

Date	Facility	Instrument	Slit Size (arcsec)	Resolving Power	$S/N \\ (\lambda = 4000 \text{Å})$	W _{Ca II K} (mÅ)	$W_{ m MgII}$ (mÅ)	[Ca/H] ^a	[Mg/H] ^a
2000.09.15	VLT	UVES	2.1	20 000	19	81 ± 13	125 ± 19	-6.9 ± 0.1	-5.5 ± 0.1
2001.09.02	VLT	UVES	2.1	20 000	18	81 ± 13	126 ± 22	-7.0 ± 0.1	-5.5 ± 0.1
2007.10.25	Magellan	MIKE	0.7	40 000	37	72 ± 7	133 ± 5	-7.1 ± 0.2	-5.6 ± 0.1
2007.10.26	Magellan	MIKE	0.7	40 000	27	75 ± 9	137 ± 6	-7.2 ± 0.1	-5.6 ± 0.1
2007.11.20	Keck	HIRES	1.1	36 000	13	74 ± 13	152 ± 9	-7.1 ± 0.2	-5.6 ± 0.1
2008.08.21	Magellan	MIKE	0.7	40 000	44	76 ± 7	144 ± 5	-7.0 ± 0.2	-5.6 ± 0.1
2009.10.14	Magellan	MIKE	0.7	40 000	38	84 ± 11	139 ± 6	-7.1 ± 0.2	-5.6 ± 0.1
2011.03.23 ^b	Keck	HIRES	1.1	36 000	14	48 ± 12	106 ± 14	-7.4 ± 0.1	-5.7 ± 0.1
2015.02.26	VLT	X-shooter	1.0	5 400	86	70 ± 7	143 ± 7	-7.1 ± 0.1	-5.5 ± 0.1
2015.11.14	Keck	HIRES	1.1	36 000	34	81 ± 6	153 ± 8	-7.0 ± 0.1	-5.6 ± 0.1

^a The listed uncertainties are rounded to the nearest 0.1 dex and include only the model fitting errors (see Section 2.2).

row. This suggests that these data are problematic owing to the high sky background, and they are disregarded in the subsequent analyses. The uncertainties in metal abundance are only formal fitting errors and do not include other potential sources of error such as systematic offsets between instruments and their processing pipelines (Koester et al. 2009). In fact, the abundance values determined using the nominal instrument resolution reveal a clear instrument dependence, with offsets up to 0.4 dex for [Ca/H] and up to 0.2 dex in [Mg/H]. In order to better understand this issue, the resolving power for the UVES and HIRES model fits was increased up to 40 000, and this was found not only to improve the agreement between all the abundance determinations, but also to better track the equivalent width measurements of both lines; these abundances are adopted here and listed in listed in Table 2. If the metal abundances in GD 56 are constant, then the mean values and their dispersions of the reliable data sets are $[Ca/H] = -7.1 \pm 0.1$, and $[Mg/H] = -5.6 \pm 0.1$.

3 DISCUSSION

The changes in absolute infrared flux of GD 56 are clear and compelling, but at the same time the flux ratios between the two shortest wavelength channels in both Spitzer and WISE are consistent with remaining constant (Figures 1–3). Concurrently, there is no indication that the photospheric line strengths or metal abundances are changing, although the sampling is relatively sparse. Based on diffusion theory, the expected sinking timescales for calcium and magnesium in a hydrogen-atmosphere white dwarf with $T_{\rm eff}=15\,000\,{\rm K}$, $\log\,g=8.0$ are 1.0 and 0.9 d respectively (Koester 2009). Thus, while the stellar photosphere should track any accretion rate changes on daily timescales or longer, none are apparent in the observations. These results are comparable to those obtained via multi-epoch spectral observations of the dusty white dwarf prototype G29-38 (von Hippel & Thompson 2007; Debes & López-Morales 2008).

These observations provide empirical constraints on the possible underlying processes in the circumstellar disk orbiting GD 56. In this section, the infrared variability and apparently constant accretion rate are discussed in the context of relevant timescales, geometry, and possible physical models. These ideas are considered in the context of other dusty systems for consistency, and with respect to disk evolution models to assess their wider applicability. The inferred, ongoing accretion rate is relevant for the following discussion, where diffusion theory predicts rates of $1.0 \times 10^8 \ g \ s^{-1}$ and

 0.6×10^8 g s⁻¹ based on the magnesium and calcium abundances, respectively, assuming they are deposited at their bulk Earth mass fractions (Allègre et al. 2001; Koester 2009).

3.1 Previous Infrared Modeling of GD 56

It is worthwhile to first review previous data and modeling of the infrared emission in the GD 56 system, as it remains unusual and to date has the largest, observed, fractional infrared luminosity of any dusty white dwarf (Rocchetto et al. 2015). Over a decade ago when GD 56 was first observed with Spitzer, it was noted that the infrared emission could not be reproduced by a flat disk alone (Jura et al. 2007). In Figure 6 these initial infrared observations are reproduced with better short wavelength data and atmospheric modeling, together with a flat disk model that fails to reproduce the IRAC flux measurements. Because it is now clear that the $3-5 \mu m$ fluxes vary over time, any disk model must be viewed with caution when applied to infrared data that are not taken simultaneously, such as those in the figure. Regardless, no flat disk model can reach the plotted fluxes, and thus this model is insufficient. A modestly warped segment was later added to the flat disk model for GD 56, and this was able to account for the overall infrared emission including its strong silicate feature (Jura et al. 2009). The source of any warping in an otherwise flat disk is unclear, but possibilities include gravitational perturbations by orbiting bodies, radiative instability (Jura et al. 2007), and dust that follows the scale height of gas.

In the lower panel of Figure 6 the stellar photosphere has been subtracted and only the face-on (flat) disk model remains with the initial IRAC data, the sole MIPS $24\,\mu m$ observation, and the HK photometry. The shaded regions give the extent of the observed variability to date in all bands with multiple measurements, where the largest variation is the 0.26 mJy peak-to-peak flux change at 4.5 μm (between 2013 Oct and 2017 Dec). While the temporal coverage in the infrared has (multi) year-long gaps, the overall behavior of the fluxes in Figure 1 suggests the variable dust emission is either stochastic, or possibly a periodic brightening followed by dimming. While radiative warping may be responsible for additional emitting surface that exceeds the intrinsic infrared brightness of a flat disk configuration, it does not necessarily follow that such a structure can cause the observed variability.

^b This exposure was completed during twilight and suffers from high background emission.

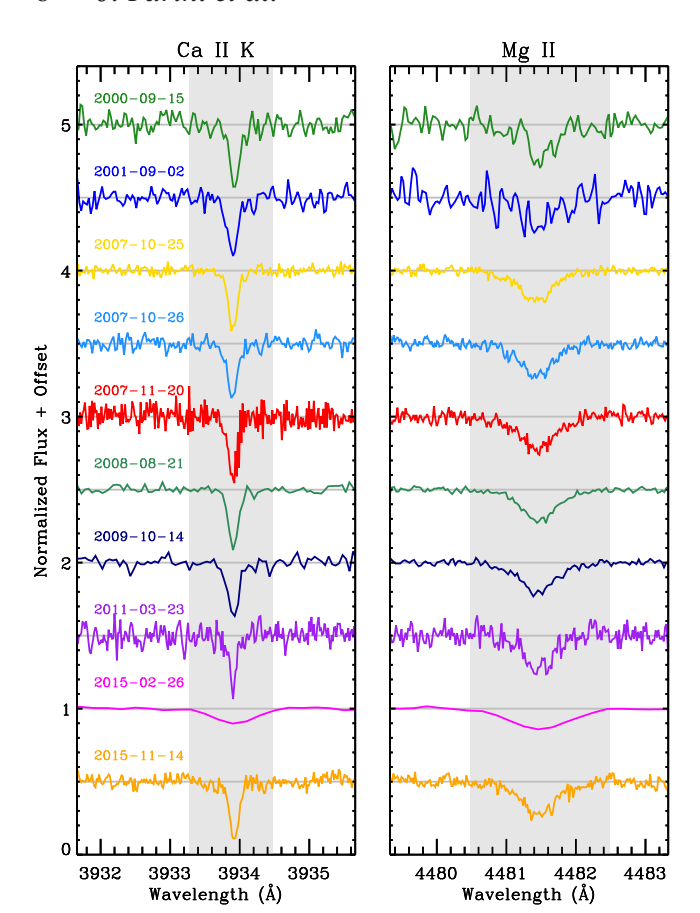


Figure 4. Multi-epoch optical spectroscopy of GD 56 in the region of the Ca π K and Mg π 4481 Å lines, with details provided in Table 2. All spectra are normalized and vertically offset for clarity, with chronological ordering from top down. The 2011 Mar 23 spectrum exhibits weaker and narrower lines, but is the result of a single exposure taken during twilight, with bright sky emission throughout the wavelength regions of interest. Hence, this may have affected the fidelity of the data during the spectral extraction process. The velocities of all absorption features are consistent within the wavelength calibration errors.

3.2 Timescale and Accretion Rate Considerations

The simplest model for the observed long-term infrared variability towards GD 56 is the production and depletion of dust clouds that provide emitting surface areas in excess of – or in lieu of – a flat disk configuration. Such clouds must not change orbital radius drastically, as this would change the dust temperature and hence the flux ratio between 3.5 and 4.5 μ m. A priori, any transient or periodic dust structure can be optically thick or optically thin, but it is noteworthy that blackbody dust with T=1000 K (Jura et al. 2007) will orbit near 1.46 R_{\odot} and thus somewhat outside the stellar Roche limit (for GD 56, asteroid-like bodies with density 3 g cm⁻³ should disrupt only within $0.9 R_{\odot}$). Before exploring possible mechanisms for dust production and depletion around GD 56 and other dusty white dwarfs, it is best to establish some theoretical context.

A good starting point is to consider the relevant physical timescales for particulate and gaseous debris in the vicinity of the Roche limit for white dwarfs, where the orbital radii are $r \approx 1.0-1.5\,R_\odot$. The timescales that govern five processes are important: Keplerian orbits, condensation, collisions, Poynting-Robertson (PR) drag, and viscous spreading. The orbital period at these radii for a $0.6\,M_\odot$ star is between 3 and 7 h, and hence

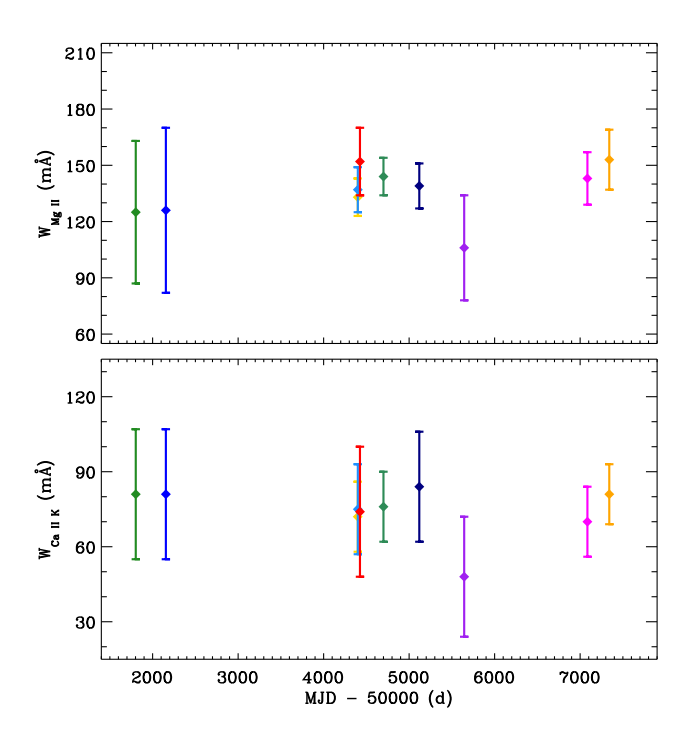


Figure 5. The measured equivalent widths of the two metal absorption features at each epoch, color-coded identically to the spectra in Figure 4. These measurements are shown with 2σ error bars and indicate that no appreciable changes are observed in metal abundance, and are thus consistent with a constant accretion rate. The purple data points corresponding to the 2011 Mar 23 data may have suffered from high background contamination and problematic sky removal.

solids will orbit at (circular) speeds exceeding 250 km s⁻¹. Condensation of metallic gas onto grains is likely to be efficient in the case of identical chemical compositions, and take place on orbital timescales or less (Metzger et al. 2012). The collisional timescale for dust in a disk-like configuration is directly comparable to the orbital period (i.e. $t_{\rm coll} \sim P/4\pi\tau$), with the optical depth $\tau \gtrsim 1$ in the case of a vertically opaque disk, and $\tau \simeq L_{\rm IR}/L_*$ if the disk is optically thin in the radial direction. A disk may be optically thick in the radial direction (due to grazing starlight), yet remain vertically optically thin and experience less frequent collisions than implied by $f = L_{\rm IR}/L_*$. For white dwarfs with well-determined fractional dust luminosities (Rocchetto et al. 2015), if their vertical optical depths are comparable to f, then collision timescales will be on the order of 1 - 20 d. This is at least two orders of magnitude shorter than the timescale for angular momentum loss by solids due to PR drag, where for 1 μ m size grains with density 3 g cm⁻³, the timescales for GD 56 are between 6 and 14 yr. For the population of known dusty white dwarfs, all with $L_{\rm IR}/L_* \gtrsim 10^{-3}$, it can be shown that for $\tau > 10^{-5}$, the collisional timescale is *always shorter* than PR drag (Farihi et al. 2008).

Before discussing the timescale for the viscous spreading of gas, the implications of collisions are considered. In the restricted case of disks that are completely optically thin, the relevant timescale for solids is thus the collisional timescale. For GD 56 this is a few orbital periods and less than 8 h within 1.5 R_{\odot} , requiring that the entire disk be replenished every few days or so, and with a dust mass production rate sufficient to maintain $L_{\rm IR}/L_* \approx 0.03$ (Rocchetto et al. 2015). This entails around 10^{18} g (Jura et al. 2009)

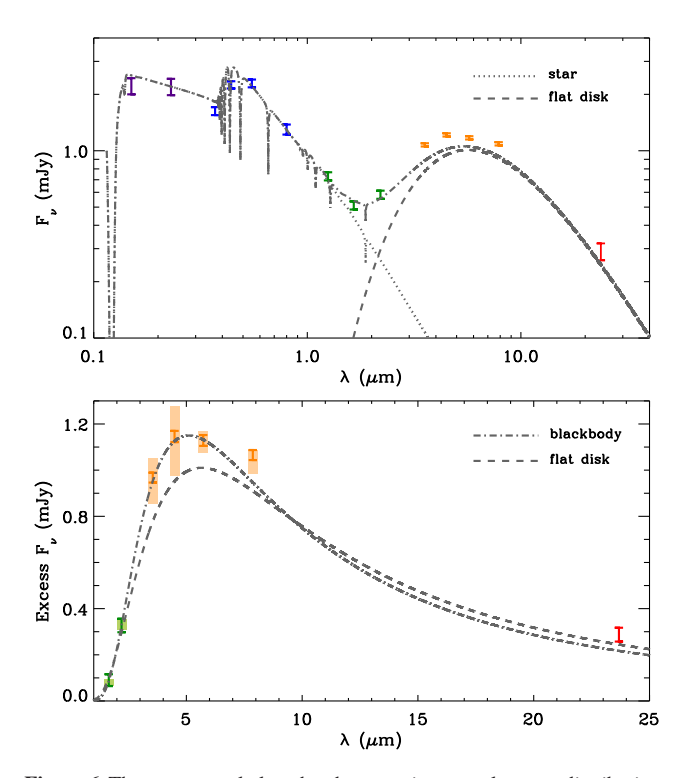


Figure 6. The upper panel plots the photometric spectral energy distribution (SED) of GD 56 from the ultraviolet through the infrared, including the first epoch of (cryogenic) IRAC data, and MIPS 24 μm flux. The short wavelength data are fitted with a stellar atmosphere model of 15 000 K (dotted line) and added to this is a flat disk with inner temperature 1400 K, outer temperature of 600 K, and zero inclination. This flat disk model is representative of the best possible fit to the data with this restricted geometry, yet cannot account for the IRAC fluxes. In the lower panel the stellar photosphere has been subtracted from the photometry, and this excess flux is plotted linearly with the same flat disk model, as well as a blackbody with T=1000 K. The shaded regions represent the range of observed infrared fluxes over 11.2 yr, where the minima at 3.6 and 4.5 μm are conceivably (just) consistent with a face-on, flat disk.

per collision timescale, which would eventually result in a mass accretion rate onto the star that is higher than 10^{12} g s⁻¹, and consistent with numerical simulations of collisional cascades around white dwarfs (Kenyon & Bromley 2017a). Such high rates of (sustained or transient) disk accretion have been suggested by theory and hinted at via observations (Rafikov 2011b; Girven et al. 2012; Kenyon & Bromley 2017b), but so far have not been confirmed by (limited) X-ray data (Farihi et al. 2018). Furthermore, the maximum accretion rate from PR drag alone acting on optically thin debris is set only by the stellar luminosity and the fraction of starlight intercepted by the disk (Bochkarev & Rafikov 2011); if all radiation from GD 56 is intercepted by dust, the maximum mass accretion rate is 3×10^{10} g s⁻¹. Thus if disks are primarily optically thin, and accretion rates do exceed this value, then collisions dominate the production of gas that eventually accretes and pollutes the star, but material must be continually supplied to the disk (Kenyon & Bromley 2017a,b).

In the context of GD 56, these potential disk implications can be compared with the stellar atmospheric data. Based on the photospheric calcium and magnesium abundances and diffusion theory (Koester 2009), the current total stellar accretion rate is $(0.8 \pm 0.2) \times 10^8$ g s⁻¹ using either of these two elements at its bulk Earth mass fraction (Allègre et al. 2001). These estimates are orders

of magnitude smaller than any of the above predictions for optically thin dust shell depletion – especially where collisions may dominate the production of gas - but agree well with model predictions for flat and opaque dust disks depleting via PR drag (i.e. no collisions (Rafikov 2011a; Bochkarev & Rafikov 2011)). Notably, this accretion rate is typical for polluted stars with metal diffusion timescales of less than a few years, where an ongoing steady state can be confidently inferred - based on diffusion theory, no system to date has been determined to substantially exceed $10^9\,\mathrm{g\,s^{-1}}$ (Farihi et al. 2016). If correct, then any long-term $(10^4 - 10^7)$ yr; Girven et al. 2012) infrared emission in dusty white dwarf systems is likely to be from solids in a flat disk, and consistent with dynamical relaxation on orbital timescales, where a sufficient component is optically thick. This represents the basic utility of the canonical flat and opaque disk model; immunity to collisional annihilation, longevity, and accretion rates that broadly match those of diffusion theory (Jura 2003; Rafikov 2011a; Metzger et al. 2012). [It is noteworthy that recent simulations by Kenyon & Bromley (2017a,b) cannot produce a vertically thin disk of material at relevant orbital distances for dusty white dwarfs, whereas analytical work (Bochkarev & Rafikov 2011; Metzger et al. 2012) appears to favor this configuration.]

While collisions can be avoided by efficient damping in a flat and opaque disk (Farihi et al. 2008; Metzger et al. 2012), once solids have been sublimated or collisionally vaporized, regardless of geometry, the material will no longer evolve via radiation forces. Prior to the accretion of material onto the stellar surface, the final relevant timescale may be set by gas viscosity. And while the properties of pure gas disks orbiting white dwarfs have been discussed at length in the literature (Jura 2008; Rafikov 2011a; Farihi et al. 2012b; Metzger et al. 2012; Kenyon & Bromley 2017b), the implications for infrared and optical variability have not been fully explored. Several estimates exist for gas viscosity in a disk dominated by metals, where the two uncertain factors are in the size of the α parameter (Shakura & Sunyaev 1973) and whether the disk is ionized or neutral. For bulk Earth material, the mean atomic weight of neutral gas would be $32.8 m_p$, and if this material is fully ionized then $16.4 m_p$. Using these two extrema yields viscous timescales in the range $(10/\alpha)$ yr $\lesssim t_V \lesssim (20/\alpha)$ yr for a typical white dwarf disk at $r = 0.2 R_{\odot}$. Only in the limit $\alpha \approx 1$ can the viscous timescale approach that of PR drag, and only then for grains larger than 1 µm (Rafikov 2011a).

Therefore, a significant time lag may result between a change in the rate of solids delivered into an inner gas disk, and a subsequent change in the mass accretion rate from this reservoir. If $\alpha \approx 0.1 - 0.4$ as inferred for a variety of fully ionized accretion disks (King et al. 2007), then the shortest realistic timescale would be $t_{\rm v} \approx 25-100\,{\rm yr}$. Therefore any changes in dust and gas production within a disk, including the inward movement of solids that eventually sublimate, can be mediated prior to accretion onto the stellar surface if an α -type gas disk is present. Any such inner disk will smooth over changes on these relatively long timescales, and no changes in accretion rate would be expected on PR drag timescales. While the presence of such inner gas disks orbiting white dwarfs is empirically unconstrained, if they are ubiquitous then changes in accretion rate might not be expected on human timescales. There are a handful of circumstellar gas detections via absorption towards polluted stars; most dramatically around WD 1145 in the optical (Xu et al. 2016; Redfield et al. 2017), and possibly via a weak circumstellar component in the Ca II H and K lines of EC 11246-2923 (Debes et al. 2012a), but also in the far-ultraviolet spectra of both SDSS 1228+1040 and PG 0853+516 (Gänsicke et al. 2012). In none of these cases do the gas velocities approach that expected for freefall, and hence the behavior of disk material prior to reaching the stellar surface is unknown. An α disk reservoir of gas is consistent with the unchanging metal lines in GD 56 and SDSS 0959, despite the changes observed in infrared emission (Xu & Jura 2014), and regardless of the exact dust production or depletion mechanisms.

Because this study considers non-canonical disk geometry and evolution for GD 56, it is worthwhile to mention the one case where a non-canonical configuration has been established. The circumbinary disk orbiting the polluted white dwarf SDSS J155720.77+091624.6 (hereafter, SDSS 1557) and its companion must be optically thin and vertically extended to account for the infrared data (Farihi et al. 2017). The system exhibits a strong infrared excess that cannot be reproduced by emission from a cool companion, and prior to the discovery of its duplicity, the infrared emission was well-matched by a face-on, flat disk model (Farihi et al. 2012a). However, the orbiting companion dynamically precludes material in the region where such a flat disk would reside, and thus the $T \approx 1100 \,\mathrm{K}$ dust emission must originate from optically thin material at $r = 3.3 R_{\odot}$ (Farihi et al. 2017). SDSS 1557 demonstrates the plausibility of a non-flat disk of material that continuously feeds atmospheric metals onto a white dwarf for at least several years.

3.3 Infrared Brightening and Dimming at GD 56

A plausible scenario for infrared variability in white dwarf dust disks is the following. There are clouds of dust that are transiently or quasi-periodically appearing and disappearing in a circumstellar environment with an underlying disk that is substantially more massive. Such a picture can account for the rapid decline of infrared flux from SDSS 0959, where the discovery observations were taken during the presence of additional clouds of material, and these were quickly re-assimilated into an existing disk. Any debris cloud generated by impact or collisions will have a range of orbits, but all will intersect that of any underlying disk, unless it occurs at the extremities. For a stray body, an impact onto the innermost edge of a particulate disk within the Roche limit is the least probable location, and requires a body or bodies smaller than a km that were immune to tidal disruption on any prior periastra (Brown et al. 2017). Unless optically thick, any transient dust cloud that is vertically offset from an extant disk plane would quickly attain a higher temperature than debris that is partly shielded from starlight.

While transient dust clouds quickly being absorbed into an existing disk may be able to account for the sparse infrared data on SDSS 0959, it may not work for GD 56 where the infrared dimming takes place over many years. It is possible, however, that a simple (re-)incorporation of material above or below the plane of an underlying disk may be a process that acts like a damped oscillator. If so, then dust clouds with relatively small masses may quickly become assimilated into a larger disk if damping is near critical, but the system may oscillate if damping is inefficient or the dust cloud mass is larger. In the canonical opaque disk, damping is sufficiently high that collisions are negligible, and (re-)condensation of gas onto a particulate disk should occur on orbital timescales (Metzger et al. 2012). This scenario might account for the disappearance of gas emission lines around SDSS J161717.04+162022.4 (Wilson et al. 2014).

In the case of GD 56, an important observational clue to the dust removal process is the fact that the flux ratios between $4.5\,\mu m$ and 3.5 μm do not change substantially. This implies the dust is created, and later destroyed or subsumed, within a range of orbital radii that does not change substantially with time. Another interesting em-

pirical indication is that the gradual decay in $3-5 \mu m$ flux around GD 56 appears to mimic that seen towards several bright debris disks orbiting young main-sequence stars, and where this decay is thought to be due to collisions of mm-size condensates (Meng et al. 2014, 2015). In these studies, the generation of extreme infrared excesses are attributed to planetary impacts. These impacts produce vaporized debris, which re-condenses and undergoes a collisional cascade that eventually depletes grains that emit efficiently in the infrared, aided by the removal of the smallest grains by radiation pressure. While the blowout of dust is not relevant for white dwarf systems, the fact that the collisions will dominate unless damped suggests the analogy here may be compelling. Removal of small grains around white dwarfs might occur via continued collisions and sputtering, but alternatively if they are heated to temperatures sufficient for rapid sublimation as may be the case for WD 1145 (Xu et al. 2018), then there could be sufficient means to destroy dust in the vicinity of where it is produced. It is noteworthy that the channel 2:1 flux ratios do not appear to change substantially between the combined IRAC and WISE epochs reported for SDSS 0959 (Xu & Jura 2014).

In further analogy with WD 1145, it is plausible that minor bodies are generating clouds of $T \approx 1000 \,\mathrm{K}$ dust around 1.46 R_{\odot} either via collisions or sublimation – but not tidal disintegration at this distance. It is now well established that the disk of dust and gas orbiting WD 1145 is eccentric (Cauley et al. 2018), and the same appears to be the case for at least two other disks (Manser et al. 2016a; Dennihy et al. 2018; Miranda & Rafikov 2018). This implies that tidal disintegration of a large body or bodies is not likely to be ongoing in a near-circular orbit at or near the Roche limit (Gurri et al. 2017; Veras et al. 2017), but instead orbiting bodies are crossing in and out of this radius. Collisions associated with circularization of a disk may produce dust periodically, some of which may be located outside of the disk plane, and later this material becomes assimilated into the evolving disk. There are a few considerations that make this scenario plausible, as long as the dust production sites are relatively localized and not varying in orbital distance on the timescales probed by the observations.

First, the circularization process is not well constrained, and material may end up over a range of orbits spanning the Roche limit. This could imply that intact bodies survive longer outside the Roche limit, and are thus available as sites of dust production. Second, the Roche limit separates disrupted and intact bodies of the same composition, but there may be a transition zone where some bodies remain intact while others are fragmented due to compositional gradients. Third, small bodies can be formed by recycled ring material at the Roche limit via disk spreading (van Lieshout et al. 2018) – as has been suggested for the rings of Saturn (Charnoz et al. 2010) – and this process might also play a role in the rise and fall of emitting dust. This latter scenario requires a massive disk in excess of a lunar mass, but at the same time GD 56 has the largest known infrared excess of any dusty white dwarf.

While somewhat speculative, the infrared data for GD 56 may hint at an overall trend that includes a flux increase followed by a gradual decay. If there is a periodic signal here, it would be crudely around 7 yr and then correspond roughly to an orbital scale of 3 AU. In this case an infrared brightening might be expected before or near 2020. It is not unreasonable that some tidally-disrupted material remains in the process of circularization, with small bodies still strung out along a range of wide orbits (Debes et al. 2012b; Veras et al. 2014), and these periodically interact with the disk around GD 56, generating dust that is eventually destroyed or re-incorporated. Another remote possibility is if a planetary body on a wider orbit has sufficient gravitational influence to induce a disk warp during periastron, it could also be that a warp may decay gradually as a damped oscillator (but in the case of GD 56 it would need to be highly inefficient with a decay timescale longer than 10³ d). White dwarf disk precession via general relativity can be on the order of years, with a steep dependence on radial distance (Miranda & Rafikov 2018), but it is unclear if this would drive a periodic warp or change in dust mass. More infrared data with better temporal coverage is required before any realistic model constraints can be made.

Lastly and importantly, the dimming trend at GD 56 after MJD 56 000 appears to be consistent with the broad behavior predicted by numerical simulations of collisional cascades around white dwarfs (Kenyon & Bromley 2017a), and more generally the predictions of steady state evolution of debris disks due to collisions (Wyatt et al. 2007). In the former simulations, the basic behavior of the infrared dust luminosity is stochastic, yet switching between high states of visibility, and non-detectable low states. Steady states are possible, or even likely with continued mass input into an existing disk, but without such input an infrared excess will decay to non-detectable levels. Nevertheless, the decay trend seen in the data for GD 56 is well within the family of predictions based on these models, and while solutions are degenerate, roughly speaking the model sets that can reproduce the infrared data have dust and gas production rates in excess of 10^{12} g s⁻¹ and total belt masses in excess of 10^{23} g (Kenyon & Bromley 2017a).

While such rates are consistent with the estimate made above based on destroying all the infrared emitting dust around GD 56 within a typical collision timescale, they are far in excess of that inferred to be ongoing via diffusion theory. Such high accretion rates, if they occur, have fundamental implications for the nature of the remnant planetary systems orbiting white dwarfs. For example, if 30% of white dwarfs with cooling ages in the range 20 – 200 Myr accrete from disks (Koester et al. 2014) that produce accretion rates as high as 10^{13} g s⁻¹, then a given system with a duty cycle of 0.3×100 Myr can have accreted up to 10^{28} g $(2 M_{\oplus})$ of material. This is in stark contrast to the consumption of a mass closer to 10²⁵ g (Pluto) based on the more sedate accretion rates inferences made from diffusion theory (Koester 2009). This potential tension between theory and observation cannot be resolved within the context of the current work, but the infrared behavior of GD 56 is a strong indication that collisions are of fundamental importance in the debris disks that orbit polluted white dwarfs.

4 SUMMARY AND CURRENT PERSPECTIVE

Infrared observations of GD 56 reveal both brightening and dimming events associated with circumstellar dust. Over a span of 11.2 yr, the 3 – 5 μ m fluxes in both *Spitzer* and *WISE* are shown to increase and decrease, where the peak-to-peak changes are over 20% and a gradual dimming is apparent for at least one and possibly two intervals. In contrast, neither the flux ratios between the two shortest wavelength channels on both spacecraft, nor the photospheric metal absorption in the star appear to be changing. These collective results suggest dust is produced and later destroyed (or subsumed) without any significant change in the range of orbital radii; i.e. PR drag is not affecting the distribution of the emitting dust. Any gas resulting from the dust production process – including small dust grains that rapidly sublimate - may quickly re-condense onto grains or join an α-like accretion disk, and this may delay changes in mass accretion rate for decades or longer. These ideas have applicability beyond GD 56 and are generally consistent with all observations to date for polluted white dwarfs from the infrared to the optical.

It is hypothesized that collisions with an existing and evolving disk may lead to infrared brightening via dust production, and, subsequently, infrared dimming as the cascade grinds down the material into sizes that do not emit efficiently at micron wavelengths. Competing effects may be present if there are massive, flat and opaque disks orbiting most polluted white dwarfs, as transient debris clouds will be readily subsumed into such an underlying disk. A canonical disk may be warped by gravitational forces, and in this way increase its emitting surface to produce infrared flux changes, but it would likely require a fairly massive orbiting body, and the observed dimming may be difficult to reconcile with such a scenario. Of all the ideas discussed here, only variable disk warping will not give rise to an eventual change in accretion rate onto the star (and in the broader context cannot account for the continued presence of gas in many debris disks orbiting polluted stars).

On the one hand, the idea that white dwarf disks are undergoing a collisional cascade is rather reasonable, and for GD 56 the infrared flux changes have clear similarities with those observed towards young, planet-forming debris disks orbiting main-sequence stars. This can also account for the continued production of gas for many stars that exhibit these features by emission or absorption or both. On the other hand, and despite broad agreement with model families of collisional cascades, the total disk masses and production rates for dust and gas are orders of magnitude higher than inferred from diffusion theory, and the disk never settles dynamically into a flat configuration. Recently, Bauer & Bildsten (2018), building on previous work (Deal et al. 2013; Wachlin et al. 2017), find ongoing accretion rates up to 10^{13} g s⁻¹ are possible if hydrogen-rich white dwarfs suffer the thermohaline instability in their mixing layers where metals are present. While this possibility has been discounted in the context of white dwarf atmospheres and diffusion theory (Koester 2015), it has clear parallels with the dust production rates via collisions discussed in this work inspired by GD 56. While diffusion theory predicts that any changes in mass accretion rates should be observable as changes in their metal absorption features over a finite number of sinking timescales, the models that include thermohaline mixing do not (Bauer & Bildsten 2018). Thus, on the one hand, accretion rate changes may be expected from diffusion theory, yet restrained by longer gas viscosity timescales. But on the other hand, even if accretion occurs directly onto the stellar surface, changes in metal abundance would not be observable if a thermohaline instability stifles diffusion.

It is ironic that this discovery comes 15 years after the launch of *Spitzer*, and towards the end of its extended, post-cryogenic lifetime. Reach et al. (2009) noted that IRAC short-cadence monitoring of G29-38 – the prototype and brightest dusty white dwarf – revealed 3 – 8 µm flux changes, but as a well-known pulsating variable of the ZZ Ceti class such changes are particularly challenging to interpret as variability in the circumstellar dust content. While likely nearing the end of their mission lifetimes, both *Spitzer* and NEOWISE currently offer the best observational constraints on the evolving and dusty planetary systems orbiting polluted white dwarfs.

ACKNOWLEDGEMENTS

The authors acknowledge useful conversations with R. Rafikov, and thank an anonymous reviewer for a careful reading of the manuscript. This work is based in part on observations made with the *Spitzer Space Telescope*, which is operated by the Jet Propulsion Laboratory, California Institute of Technology under a contract with NASA. This publication makes use of data products from the

Wide-field Infrared Survey Explorer, which is a joint project of the University of California, Los Angeles, and the Jet Propulsion Laboratory / California Institute of Technology, funded by the NASA. Some of the data presented herein were obtained at the W. M. Keck Observatory from telescope time allocated to NASA through scientific partnership with the California Institute of Technology and the University of California. This work was supported by a NASA Keck PI Data Award, administered by the NASA Exoplanet Science Institute. Some of the observations presented here were made with ESO Telescopes at the Paranal Observatory. JF acknowledges support from STFC grant ST/R000476/1. RvL was supported by the DISCSIM project, grant agreement 341137 funded by the European Research Council under ERC-2013-ADG. TGW wishes to acknowledge funding from a STFC studentship, and OT was partially supported by a Leverhulme Trust Research Project Grant. Research leading to these results has received funding from the ERC under the European Union's 7th Framework Programme no. 320964 (WDTracer). TvH was supported by the National Science Foundation Award AST-1715718, and AB acknowledges the support of a Royal Society Dorothy Hodgkin Fellowship.

REFERENCES

Allègre C., Manhès G., Lewin É. 2001, Earth Planetary Sci. Letters, 185, 49 Apai D., et al. 2017, Science, 357, 683

Bauer E. B., Bildsten L. 2018, ApJ, 859, L19

Bochkarev K. V., Rafikov R. R. 2011, ApJ, 741, 36

Boyajian T. S., et al. 2018, ApJ, 853, L8

Brown J. C., Veras D., Gänsicke B. T. 2017, MNRAS, 468, 1575

Cauley W. P., Farihi J., Redfield S., Bachmann S., Parsons S. G., Gänsicke B. T. 2018, ApJ, 852, L22

Charnoz S., Salmon J., Crida A., 2010, Nature, 465, 752

Deal M., Deheuvels S., Vauclair G., Vauclair S., Wachlin F. C. 2013, A&A, 557, L12

Debes J. H., López-Morales M. 2008, ApJ, 747, 148

Debes J. H., Kilic M., Faedi F., Shkolnik E. L., Lopez-Morales M., Weinberger A. J., Slesnick C., West R. G. 2012a, ApJ, 754, 59

Debes J. H., Walsh K., Stark C. 2012, ApJ, 747, 148

Dennihy E., Clemens J. C., Dunlap B. H., Fanale S. M., Fuchs J. T., Hermes J. J. 2018, ApJ, 854, 40

Farihi J. 2009, MNRAS, 398, 2091

Farihi J. 2016, New Astronomy Reviews, 71, 9

Farihi J., Gänsicke B. T., Steele P. R., Girven J., Burleigh M. R., Breedt E., Koester D. 2012, MNRAS, 421, 1635

Farihi J., Gänsicke B. T., Wyatt M. C., Girven J., Pringle J. E., King A. R. 2012, MNRAS, 424, 464

Farihi J., Koester D., Zuckerman B., Vican L.; Gänsicke B. T., Smith N., Walth G., Breedt E. 2016, MNRAS, 463, 3186

Farihi J., Parsons S. G., Gänsicke B. T. 2017, Nature Astronomy, 1, 32

Farihi J., Zuckerman B., Becklin E. E. 2008, ApJ, 674, 431

Farihi J., et al. 2018, MNRAS, 474, 947

Fazio G. G., et al. 2004, ApJS, 154, 10

Freudling W., Romaniello M., Bramich D. M., Ballester P., Forchi V., García-Dabló C. E., Moehler S., Neeser M. J. 2013, A&A, 559, A96

Gaia Collaboration; Brown, A. G. A., Vallenari A., Prusti T., de Bruijne J. H. J., Babusiaux C., Bailer-Jones C. A. L. 2018, A&A, in press (arXiv;180409365)

Gänsicke B. T., Koester D., Farihi J., Girven J., Parsons S. G., Breedt E. 2012, MNRAS, 424, 333

Gänsicke B. T., Koester D., Marsh T. R., Rebassa-Mansergas A., Southworth J. 2008, MNRAS, 391, L103

Gänsicke B. T., et al. 2016, ApJ, 818, L7

Gianninas A., Bergeron P., Ruiz M. T. 2011, ApJ, 743, 2011

Girven J., Brinkworth C. S., Farihi J., Gänsicke B. T., Hoard D. W., Marsh T. R., Koester D. 2012, ApJ, 749, 154 Gurri P., Veras D., Gänsicke B. T. 2017, MNRAS, 464, 321

Hodgkin S. T., Irwin M. J., Hewett P. C., Warren, S. J. 2009.MNRAS, 394, 675

Hughes A. M., Duchene G., Matthews B. 2018, ARA&A, in press (arXiv:1802.04313)

Jarrett T. H., et al. 2011, ApJ, 735, 112

Jura M., Farihi J., Zuckerman B. 2007, ApJ, 663, 1285

Jura M. 2003, ApJ, 584, L91

Jura M. 2008, ApJ,135, 1785

Jura M., Farihi J., Zuckerman B. 2009, AJ, 137, 3191

Kelson D. D. 2003, PASP, 115, 688

Kelson D. D., Illingworth G. D., van Dokkum P. G., Franx M. 2000, ApJ, 531, 159

Kenyon S., Bromley B. 2017a, ApJ, 844, 116

Kenyon S., Bromley B. 2017b, ApJ, 850, 50

Kiefer F., Lecavelier des Etangs A., Augereau J. C., Vidal-Madjar A., Lagrange A. M., Beust, H. 2014, A&A, 561, L10

Kiefer F., Lecavelier des Etangs A., Boissier J., Vidal-Madjar A., Beust, H., Lagrange A. M., Hébrard G., Ferlet R. 2014, Nature, 514, 462

King A. R., Pringle J. E., Livio M. 2007, MNRAS, 376, 1740

Koester D. 2009, A&A, 498, 517

Koester D. 2010, In Memorie della Societa Astronomica Italiana, 81, 921

Koester D. 2015, 19th European Workshop on White Dwarfs, ASP Conference Series 493 (San Francisco: ASP), 129

Koester D., Gänsicke B. T., Farihi J. 2014, A&A, 566, A34

Koester D., Rollenhagen K., Napiwotzki R., Voss B., Christlieb N., Homeier D., Reimers D. 2005, A&A, 432, 1025

Koester D., Voss B., Napiwotzki R., Christlieb N., Homeier D., Lisker T., Reimers D., Heber U. 2009, A&A, 505, 441

Leggett S. K., et al. 2006, MNRAS, 373, 781

Louden T., Wheatley P. J. 2015, ApJ, 814, L24

Mainzer A., et al. 2011, ApJ, 731, 53

Manser C. J., Gänsicke B. T., Koester D. Marsh T. R., Southworth J. 2016b, MNRAS, 462, 1461

Manser C. J., et al. 2016a, MNRAS, 455, 4467

Meng H. Y. A, et al. 2014, Science, 345, 1032

Meng H. Y. A, et al. 2015, ApJ, 805, 77

Melis C., Zuckerman B., Rhee J. H., Song I., Murphy S. J., Bessell M. S. 2012, Nature, 487, 74

Metzger B. D., Rafikov R. R., Bochkarev K. V. 2012, MNRAS, 423, 505

Miranda R., Rafikov R. R. 2018, ApJ, 857, 135

Rafikov R. R. 2011, ApJ, 732, L3

Rafikov R. R. 2011, MNRAS, 416, L55

Rappaport S., Gary B. L., Kaye T., Vanderburg A., Croll B., Benni P., Foote J. 2016, MNRAS, 458, 3904

Rappaport S., et al. 2018, MNRAS, 474, 1453

Reach W. T., et al. PASP, 117, 978

Reach W. T., Lisse C., von Hippel T., Mullally F. 2009, ApJ, 693, 697

Redfield S., Farihi J., Cauley W. P., Parsons S. G., Gänsicke B. T., Duvvuri G. M. 2017, ApJ, 839, 42

Rocchetto M., Farihi J., Gänsicke B. T., Bergfors C. 2015, MNRAS, 449, 574

Shakura N. I., Sunyaev R. A. 1973, A&A, 24, 337

Skrutskie M. F., et al. 2006, AJ, 131, 1163

Snellen I. A., et al. 2014, Nature, 509, 63

Vanderburg A., et al. 2015, Nature, 526, 546

van Lieshout R., Kral Q., Charnoz S., Wyatt M. C., Shannon A. 2018, MNRAS, in press (arXiv:1805.04429)

van Lieshout R., Rappaport S. 2017, in Deeg H. J., Belmonte J. A., eds, Handbook of Exoplanets. Springer International Publishing, Switzerland (arXiv:1708.00633)

Veras D., Carter P. J. Leinhardt Z. M., Gänsicke B. T. 2017, MNRAS, 465, 1008

Veras D., Leinhardt Z. M., Bonsor A., Gänsicke B. T. 2014, MNRAS, 445, 2244

von Hippel T., Thompson S. E. 2007, ApJ, 661, 477

Wachlin F. C., Vauclair G., Vauclair S., Althaus L. G. 2017, A&A, 601, A13 Welsh B. T., Montgomery S. L. 2018, MNRAS, 474, 1515

Werner M. W., et al. 2004, ApJS 154, 1

Wilson D. J., Gänsicke B. T., Koester D., Raddi R., Breedt E., Southworth J., Parsons S. G. 2014, MNRAS, 445, 1878

Wright E. L., et al. 2010, AJ, 140, 1868

Wyatt M. C., Farihi J., Pringle J. E., Bonsor A. 2014, MNRAS, 439, 3371

Wyatt M. C., Smith R., Greaves J. S., Beichman C. A., Bryden G., Lisse C. M. 2007, ApJ, 658, 569

Wyatt M. C., van Lieshout R., Kennedy G. M., Boyajian T. S. 2018, MNRAS, 473, 5286

Xu S., Jura M. 2014, ApJ, 792, L39

Xu S., et al. 2018, MNRAS, 474, 4795

Xu S., Jura M., Dufour P., Zuckerman B. 2016, ApJ, 816, L22

This paper has been typeset from a $\ensuremath{\text{TEX/IATeX}}$ file prepared by the author.